Journal of Physics and Chemistry of Solids 208 (2026) 113190

Contents lists available at ScienceDirect

Journal of Physics and Chemistry of Solids

journal homepage: www.elsevier.com/locate/jpcs

Atomic theory of point defect assisted carrier recombination in $Rb_3Sb_2I_9$

Blair R. Tuttle [a,*], Evan J. Payne [a], Zachery J. Willard [a], Sanjay V. Khare [b], Vincenzo Pecunia [c]

[a] Department of Physics, Penn State Behrend, Erie, PA, 16563, USA
[b] Department of Physics, University of Toledo, Toledo, OH, 43606, USA
[c] School of Sustainable Energy Engineering, Simon Fraser University, Surrey, BC, V3T 0N1, Canada

A B S T R A C T

Rubidium Antimony Iodide (**$Rb_3Sb_2I_9$**) is on the frontier of perovskite-inspired halide semiconductor research, with its lead-free nature and optoelectronic properties pointing to its significant potential for various energy harvesting and sensing applications. However, the performance bottlenecks that have emerged from **$Rb_3Sb_2I_9$** device studies to date highlight the importance of identifying its defect states that act as recombination centers. Here we examine the structure, energetics and electronic properties of intrinsic point defects using *ab initio* density functional methods. Rubidium vacancies and interstitials are found to be common defects, but they have very shallow gap states and may not enhance recombination significantly beyond that of bulk effects. In contrast, iodine vacancies are also common but are deep defects whose recombination behavior may be important in many circumstances. Our energy calculations for iodine vacancies quantitatively match several experiments. Strategies are suggested for ameliorating these defects in order to move $Rb_3Sb_2I_9$ toward realizing its full potential.

1. Introduction

Ternary metal halides are being developed for energy harvesting, opto-electronics and other semiconductor device applications [1]. Lead halide perovskites have shown great promise in opto-electronics (e.g. photovoltaics) due to many factors including defect tolerance [2]. The toxicity of lead, however, has motivated the search for alternative lead-free metal halide semiconductors [3,4] including the $M_3E_2X_9$ class of compounds [4–6] where M is a large singly valent cation (e.g. Cs, Rb, Tl), E is a large pnictogen [4] (As, Sb, Bi) and X is a halide element (Cl, Br, I). Recent improvements in the growth of $Rb_3Sb_2I_9$ thin films [7,8] has motivated new interest in this particular $M_3E_2X_9$ material, which has been studied for applications including photovoltaics [7,9–12], photo-detectors [13] and radiation detectors [14]. Due to its $\approx 2\ eV$ absorption gap, $Rb_3Sb_2I_9$ may be most suitable as top layer in tandem photocells or for indoor photovoltaics, an application area of growing interest due to the rising Internet of Things [15–17]. The initial solar photovoltaic conversion efficiencies reported are less than 2 % (0.66 % [10], 0.76 % [12], 1.35 % [7]) with defect-enhanced recombination limiting carrier lifetimes. However, the spectroscopic limited maximum efficiency of photovoltaic devices based on the $Rb_3Sb_2I_9$ absorber are greater than 45 % under indoor illumination, while experimentally demonstrated external quantum efficiencies are up to 65 % [7], indicating $Rb_3Sb_2I_9$ has significant potential for opto-electronic and energy harvesting applications.

Microcrystalline thin films of $Rb_3Sb_2I_9$ have been grown using a variety of methods including low temperature, solution-based processes [7,10,12] and a relatively high temperature annealing of powder precursors [18]. $Rb_3Sb_2I_9$ has a two-dimensional layered structure including staggered sheets of corner sharing $[SbI_6]^{-3}$ ionic octahedra mixed with ionic $[Rb]^{+1}$, as determined by X-ray diffraction (XRD) experiments [19]. From optical absorption spectra, the band gap of $Rb_3Sb_2I_9$ has been found to be just larger than 2.0 eV (2.03 eV [12,18], 2.04 eV [8] and 2.24 eV [10,20]). Shallow excitons are found from photo-luminescence and their binding energies are $\approx 0.1\ eV$. [12,13,18] Luminescence spectra from two independent studies suggest deep defect levels lying $\approx 1.6\ eV$ from a band edge of the $Rb_3Sb_2I_9$ bulk crystal [10,13]. In another study, analysis of photo-induced current transient (PICT) spectra suggests a trap level $\approx 0.55\ eV$ from a band edge in samples which displayed near intrinsic electrical behavior [11].

Despite the growing interest in $Rb_3Sb_2I_9$ and recent evidence of carrier lifetime limiting defects, the fundamental properties of intrinsic defects (at dilute concentrations) have not been established theoretically. Here we present a comprehensive study of the properties of intrinsic point defects in $Rb_3Sb_2I_9$ orthorhombic crystals. We have calculated the formation energy for all intrinsic defects including antisite substitutional defects, vacancies and interstitials. For typical growth conditions, we find that rubidium (Rb) vacancies and interstitials are prevalent defects. As expected from electronic structure consider-

* Corresponding Author.
E-mail address: brt10@psu.edu (B.R. Tuttle).

https://doi.org/10.1016/j.jpcs.2025.113190
Received 16 July 2025; Received in revised form 4 September 2025; Accepted 6 September 2025
Available online 9 September 2025

ations, *Rb* vacancies favor the −1 charge state, whereas *Rb* interstitials favor the +1 state and both have shallow defect levels which only weakly trap free carriers. Iodine vacancies are also a common defect and they favor the +1 charge state and have deep trap levels. From configuration coordinate diagrams, we show that the energetics of iodine vacancies match those of recent luminescence [10,13] and PICT [11] spectra. Carrier recombination at iodine vacancies may be a limiting factor for many applications. Finally, we identify challenges and opportunities for reducing iodine vacancies to help improve the optoelectronic behavior of $Rb_3Sb_2I_9$-based devices.

2. Methods

To determine the electronic structure and energetics of $Rb_3Sb_2I_9$ and defects therein, we employ the Vienna Ab Initio Simulation Package (VASP [43], [44] version 6.4.1) for density functional calculations [21,22]. For our initial total energy calculations, we treat exchange-correlation effects within the semi-local approximation optimized for solid state systems (PBEsol) [23,24]. Standard PAW potentials are used to represent the core-electrons, [45], [46] and the valence electrons included are ($4s^2$ $4p^6$ $5s^1$), ($5s^2$ $5p^3$) and ($5s^2$ $5p^5$) for rubidium (Rb), antimony (Sb), and iodine (I), respectively. The plane-wave basis function cutoff energy is set to a standard high precision value, $E_c = 220\ eV$ (see supplemental section Table S0 for convergence test results.) For Brillouin zone integrations, converged k-point meshes are employed; only the Γ point is needed for converged supercell calculations. Atomic positions are relaxed until forces reach a tolerance of 0.02 eV/Å.

The main goal of this study is to determine which isolated intrinsic point defects are electrically active in $Rb_3Sb_2I_9$. In most growth scenarios, the concentration of point defects is governed by thermodynamics and the defect's formation energy. The first principles' method for calculating point defect formation energies has been well established, as discussed in several reviews over the years [25–27]. For an intrinsic defect D in charge state q in $Rb_3Sb_2I_9$, the formation energy $(E_f[D^q])$ equation is

$$E_f[D^q] = E_{tot}[D^q] - E_{tot}[bulk] - \Delta n_{Rb}\mu_{Rb} - \Delta n_{Sb}\mu_{Sb} - \Delta n_I\mu_I + q(E_{VBM} + E_F + \Delta V) + E_{corr}$$

where $E_{tot}[D^q]$ is the energy of the periodic supercell for the bulk $Rb_3Sb_2I_9$ crystal with point defect $[D]$; E_F is the electronic Fermi energy which is a free parameter that typically varies from 0 to the band gap value; $E_{tot}[bulk]$ is the energy of the periodic supercell for the bulk $Rb_3Sb_2I_9$ crystal; Δn values are the change in the number of an atomic species between the crystalline supercell and the supercell with a point defect; the chemical potentials $[\mu]$ are set to the energy of the respective pure bulk values; E_{VBM} is the energy of the valence band maximum of the bulk $Rb_3Sb_2I_9$ crystal. These quantities are all calculated with VASP. Finally, ΔV & E_{corr} are finite size correction terms calculated using the methods developed by Freysoldt and others [28–30], as implemented in Freysoldt's code SxDefectAlign. Overall, we estimate the uncertainty is less than $\pm 0.1\ eV$ for the presently reported defect formation energy results - in supplemental section S1, we provide data supporting our estimated convergence of the formation energy calculations.

3. Preliminary results

Preliminary results for the fundamental properties for the bulk crystal include lattice vectors, bonding, chemical potential phase diagram, and electronic properties, including the band gap and the dielectric constants. When possible, these results are compared with experiments and previous calculations.

3.1. bulk properties

The structural properties of bulk crystalline $Rb_3Sb_2I_9$ has been well established previously. $Rb_3Sb_2I_9$ can exist in both the monoclinic and (nearly) orthorhombic phases. However, recently grown samples examined with X-ray diffraction (XRD) finds that $Rb_3Sb_2I_9$ favors the orthorhombic unit cell with space group $P2_1/n$ [18,19]. Starting with the primitive cell found experimentally [19], we relax the atomic coordinates and volume simultaneously. Using the PBEsol method, we find lattice constants of $a = 14.49$ Å, $b = 8.10$ Å, and $c = 20.57$ Å with unit cell angles $\alpha = \gamma = 90°$ and $\beta = 89.3°$. These results are very close (within 1 %) to their respective experimental values [18,19]. A monoclinic unit cell ($\beta \sim 125°$) has also been investigated. The bonding and lattice vectors are very similar between the monoclinic and the orthorhombic cells. With PBEsol at zero Kelvin, we find that $Rb_3Sb_2I_9$ marginally favors the orthorhombic cell by less than 1 *meV* per formula unit. The rest of this study employs only the orthorhombic structure.

Fig. 1 shows the primitive unit cell for $Rb_3Sb_2I_9$. The two-dimensional layers of connected $[SbI_6]^{-3}$ octahedra form in the (a,b) plane. $Rb_3Sb_2I_9$ has a mixture of ionic and covalent bonding with two-dimensional layers of corner sharing $[SbI_6]^{-3}$ ionic octahedra. Each antimony atom has a nominal $+3e$ charge, and each iodine has $-1e$. Of the six covalent (Sb,I) bonds, three have lengths of ≈ 2.89 Å and three have longer lengths (3.12 − 3.16 Å). The antimony centered (I,Sb,I) bond angles are close to 90 and 180°. The lattice also includes rubidium atoms in the +1e ionic state. These Rb atoms mainly interact ionically with the $[SbI_6]^{-3}$ octahedra. For each Rb atom, there are eight nearest iodine atoms, each between 3.65 − 4.03 Å away; four being less than 3.75 Å and four greater than 3.82 Å. There are two distinct types of iodine sites present. Two thirds of the iodine sites (labelled I1 below) involve one (I,Sb) bond with a ≈ 2.9 Å bond length. These iodine atoms are at the surfaces of the two-dimensional layers (see Fig. 1). One third of the iodine sites (labelled I2 below) involves two covalent (I,Sb) bonds each ≈ 3.15 Å long. These iodine atoms serve to connect adjacent $[SbI_6]^{-3}$ octahedra (see Fig. 1). The bond length values found in this study are very close to the experimental values (for comparison see Table S2 of the supplemental section of Ref. [19]).

The electronic properties of $Rb_3Sb_2I_9$ have been calculated at the PBEsol level of theory. The band structure reported in the supplemental section (see Supplemental Fig. S2) shows rather flat bands consistent with the large primitive cell. We find there is a direct gap at Γ with $E_g = 1.81\ eV$. The atom localized density of states (see Supplemental Fig. S2) shows that Sb–I molecular states dominate the band edges. These results are similar to previous electronic structure calculations for the monoclinic $Rb_3Sb_2I_9$ unit cell [10].

For defect properties we employ both semi-local (PBEsol) and hybrid-functional calculations. Specifically, we calculate the $Rb_3Sb_2I_9$ properties using the (HSE) hybrid exchange method [32,33] involving a screening parameter of 0.2 $Å^{-1}$, an exact-exchange fraction (AEXX) of 0.25 and PBEsol for the 0.75 fraction of local exchange. In addition, spin orbit coupling (SOC) is included using standard practices [34]. We find the HSE-SOC direct band gap is 2.07 *eV*, close to values found experimentally (2.03 eV [11,14] and 2.24 eV [9,16]). For the $Rb_3Sb_2I_9$ bulk crystal, the PBEsol band gap underestimation is only ≈ 0.26 *eV*, or 13%. This band gap underestimation for $Rb_3Sb_2I_9$ is significantly smaller than typically found for semiconductors (≈ 50 %) but similar to what was previously found for $AgBiI_4$ [35,36]. Using the average electrostatic potential as a common reference, we determine the relative HSE06-SOC and PBEsol band edges for the $Rb_3Sb_2I_9$ bulk. We find the HSE-SOC valence band maximum is 0.16 eV lower and the conduction band minimum is 0.11 eV higher than from the PBEsol calculations. These modest offsets will be used in the PBEsol defect energy calculations reported below.

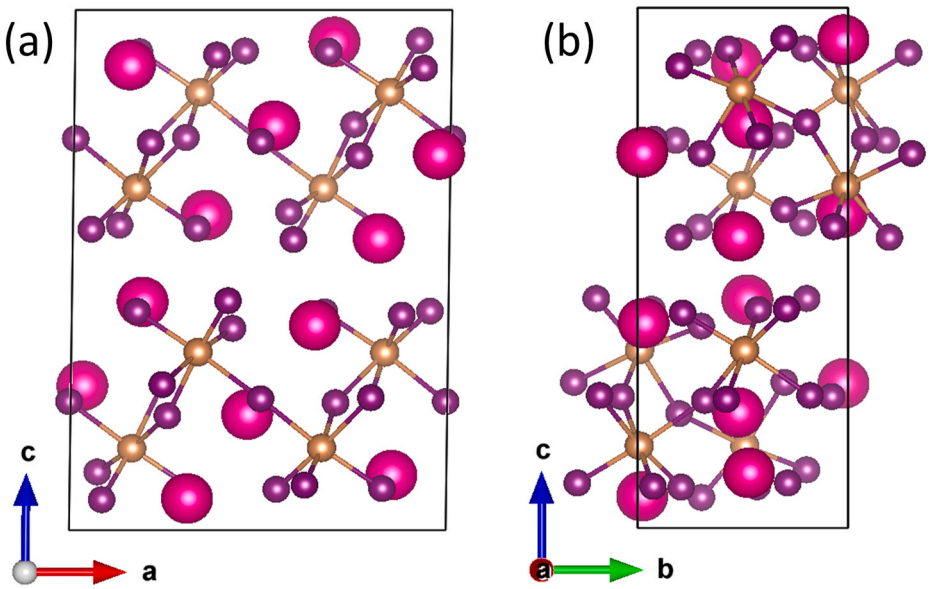

Fig. 1. Ball and stick representation of the unit cell of $Rb_3Sb_2I_9$ in the (a) plane of (c, a) and (b) in the plane of (c, b). Large pink balls are rubidium atoms, the small gold balls are antimony, and the small purple balls are iodine. The ball-and-stick model images were generated with the VESTA program [31]. (For interpretation of the references to colour in this figure legend, the reader is referred to the Web version of this article.)

Dielectric properties are important for many scientific and engineering fields. For finite supercell energy corrections (ΔV & E_{corr}) applied below, it is important to know how charged defects are screened by the dielectric medium of the bulk material. We have calculated the dielectric tensor at the PBEsol level of theory. The dielectric tensor is nearly isotropic: $\epsilon_{xx} = 10.9, \epsilon_{yy} = 10.7$, $\epsilon_{zz} = 10.3$ and $\epsilon_{xz} = \ - \ 0.1$. Static electronic and ionic dielectric values are calculated within perturbation theory [37] and found to contribute about equally to the overall dielectric tensor values. These dielectric tensor values are similar to those of other photovoltaic semiconductors, e.g. silicon with $\epsilon \approx 12$.

3.2. phase stability and range of chemical potentials

The chemical potential (μ) values are important for determining formation energies of intrinsic defects (see Equation for E_f above). As discussed in detail previously [25,26], the range of chemical potential values is constrained by the stable growth conditions of the $Rb_3Sb_2I_9$ crystal. Fig. 2 is the HSE-SOC results for the 2D phase stability plot for $Rb_3Sb_2I_9$ showing the range of chemical potentials for which $Rb_3Sb_2I_9$ is thermodynamically stable. The chemical potential variables in Fig. 2 are related to the variables in formation energy equation by the following

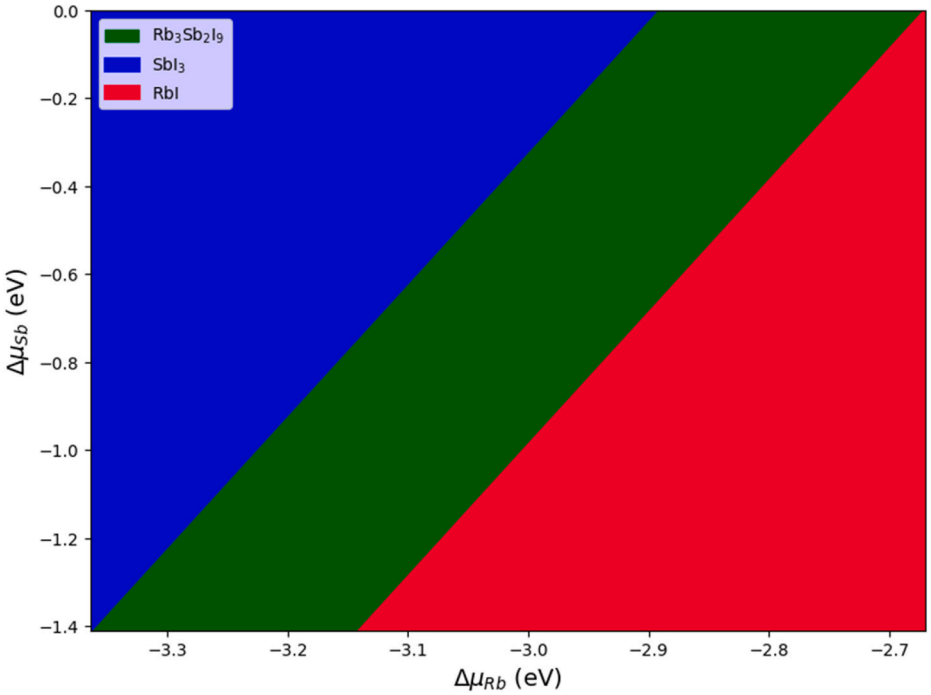

Fig. 2. Chemical stability plot of $Rb_3Sb_2I_9$. The corners of the stable region (in green) can be written in terms of the $(\Delta\mu_{Rb}, \Delta\mu_{Sb}, \Delta\mu_I)$ values (in eV) which are for top left, top right, bottom left and bottom right to be (−2.894, 0.0, −0.483), (−2.670, 0.0, −0.558), (−3.364, −1.410, −0.013), and (−3.140, −1.410, −0.088), respectively. (For interpretation of the references to colour in this figure legend, the reader is referred to the Web version of this article.)

definitions:

$$\mu_{Rb} = E_{Rb} + \Delta\mu_{Rb}\ ;\ \mu_{Sb} = E_{Sb} + \Delta\mu_{Sb}\ ;\ \mu_I = E_I + \Delta\mu_I$$

where E_{Rb}, E_{sb} and E_I are the energy of bulk Rb, Sb and I, respectively, which are calculated at both the semi-local PBEsol and the hybrid HSE-SOC levels. The full phase stability diagram is calculated using the software package pydefect [29] and reported in Supplemental Fig. S3, which shows that the PBEsol and HSE-SOC results are very similar. The stability plots include the energy for the bulk phases (Rb, Sb and I) and the stable binary phases (SbI_3, RbI_3 and RbI). The two dimensional version of Fig. S3 is shown here in Fig. 2. The $Rb_3Sb_2I_9$ stable phase region is narrow with $\Delta\mu_I$ and $\Delta\mu_{Rb}$ varying by less than 0.4 eV and $\Delta\mu_{Sb}$ extending from 0 to almost 1.4 eV. Although not shown in Fig. 2, for $\Delta\mu_{Sb} < -1.4\ eV$ the binary RbI_3 is the most stable phase (see Supplemental Fig. S3). The present phase stability plots (Fig. 2 and S3) are all very similar to a previously reported stability diagram for $Rb_3Sb_2I_9$ in the monoclinic phase [12]. The present study is for the orthorhombic phase only, but the two phases are close in structure and energy.

4. Defect results

For defect calculations, we employ supercells in order to model the isolated, dilute point defects observed experimentally. All defects properties are first calculated at the PBEsol level using a large supercell whose lattice vectors are 2, 3, and 1 times the primitive unit cell a, b and c vectors, respectively. This model will be referred to as the $2 \times 3 \times 1$ supercell. In the supplemental section, Fig. S0 shows atomic positions of the $2 \times 3 \times 1$ supercell model. The $2 \times 3 \times 1$ supercell has 24 $Rb_3Sb_2I_9$ units and lattice vectors between $25 - 30$ Å. Therefore, a single defect in a $2 \times 3 \times 1$ supercell represents a literal concentration of $6.9x10^{19}\ cm^{-3}$. However, as noted in the Methods section, we have applied techniques for removing the periodic interactions for charged defects and estimate the formation energies calculated here are within $\pm$ 0.05 eV of the results for dilute concentrations, i.e. these results are valid for a much lower concentration of defects.

To test these PBEsol defect calculations, we also perform selective calculations using a $1 \times 2 \times 1$ supercell which includes 8 $Rb_3Sb_2I_9$ units. The $1 \times 2 \times 1$ supercell defect properties are calculated at both the PBEsol and HSE-SOC levels. In all defect calculations, all atoms are allowed to fully relax for each defect and the supercell lattice vectors are fixed at their bulk values. Spin polarization is included in cases with odd number of electrons: vacancies and the interstitials.

For our calculations of a dilute defect, we introduce a single point defect into the $Rb_3Sb_2I_9$ $2 \times 3 \times 1$ supercell shown in Fig. S0. The defects considered include anti-site substitutional, vacancy and interstitial defects. There are six substitutional defects, e.g. a rubidium atom in the crystalline site of an iodine atom (Rb_I). There are 4 vacancy defects created by removing an atom, e.g. a rubidium vacancy (Va_{Rb}). Numerous interstitial sites were considered for each atom including both split interstitial and open interstitial sites. Low energy open interstitial sites were found by placing an atom at a location in the crystal corresponding to a local minimum in the crystal's electron density. The lowest energy sites were in between the two-dimensional layers of $[SbI_6]^{-3}$ octahedra. Split interstitials were found to be significantly higher in energy ($> 1\ eV$) than open interstitials. One low energy interstitial site (labelled $i1$) initially has two nearby iodine and one nearby rubidium as shown in Fig. 3 while the other low energy interstitial site (labelled $i2$) is in an open region surrounded by 6 iodine atoms. The final interaction distances between the interstitial atom and the neighboring atoms depend on the element and its charge state. Interstitial diffusion is likely to be preferentially restricted to the (a-b) plane.

4.1. neutral defect electronic structure

For each defect considered, the gap levels for the neutral defect were calculated at the PBEsol [24] level and are reported in Fig. 4. As mentioned in the Methodology section, there are two iodine sites to consider. Most defects include both occupied levels (filled circles) and empty levels (open circles) in the band gap. One case (I_{Rb}) has only one empty level in the gap whereas two defects (Rb_I & Rb_{Sb}) have only one filled level in the gap. The interstitial eigenvalues are similar for sites 1 and 2 and only one case is shown in Fig. 4.

The gap levels in Fig. 4 for the neutral defects provide an explanation of the charge states that the defect will favor for various Fermi level (E_F) values. For instance, we expect antimony interstitials (Sb_i) to favor the $+3$ charge state for E_F near the valence band edge since Sb_i has three occupied states in the upper portion of the band gap. Rubidium interstitials (Rb_i) are expected to favor the $+1$ charge state for most E_F values since Rb_i has one occupied state near the conduction band edge. These interstitial results are consistent with the ionic character of antimony and rubidium. The precise thermodynamic charge transition energies will depend on the relative relaxed energies of a defect for varying charge states, as discussed below.

From Fig. 4, we can qualitatively assess the effectiveness of each defect as a recombination center. The rubidium vacancy (Va_{Rb}), interstitial (Rb_i) and antimony substitutional (Rb_{Sb}) all have shallow defect levels and are predicted not to be efficient trapping centers. Charged carriers trapped at these defects will be easily re-emitted into the nearby band states. These shallow defects experience little structural relaxation upon charging. For example, when a neutral rubidium vacancy accepts an electron to become negatively charged, the energy of relaxation is only 0.02 eV. Electron-hole recombination through these defects will be similar to the self-trapped hole or band-to-band recombination. In contrast, the other defects with states closer to the middle of the gap are

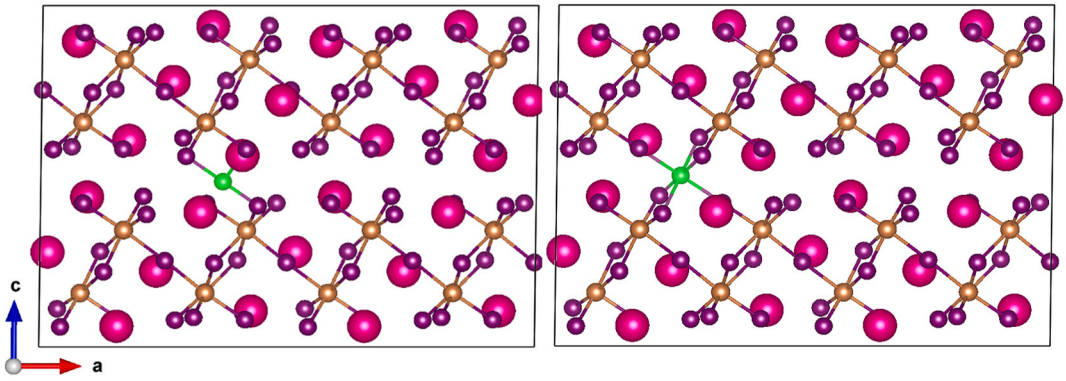

Fig. 3. The location of the open interstitial is given by the light green ball, while pink, gold and purple balls represent Rb, Sb and I atoms, respectively. Interstital site 1 is on the left whereas site 2 is on the right side of the figure. (For interpretation of the references to colour in this figure legend, the reader is referred to the Web version of this article.)

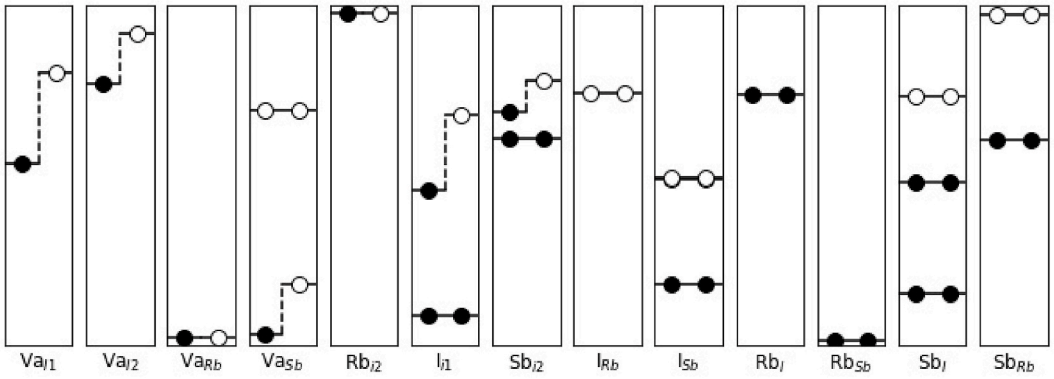

Fig. 4. Plots of the eigen-levels for neutral defects in between the valence band maximum and conduction band minimum from PBEsol results. Filled circles are occupied states and open circles are unoccupied states. The differentiated spin up and down levels are connected by a dashed line.

predicted to be effective trapping centers and candidates for defect-assisted recombination, as discussed in more detail below. For instance, the iodine vacancies (Va_I) result in a deep defect state associated with an antimony dangling bond. Upon charging, the Va_I has large lattice relaxations ($> 0.4\ eV$), typical of deep center defects.

To further illustrate the nature of the defect states, we present the defect level charge iso-surfaces in Fig. 5. These calculations employ the $2 \times 3 \times 1$ supercell and the PBEsol functional. The delocalized bulk states at the valence (conduction) band edge are shown in Fig. 5(a)(b). The valence band state is mainly a combination of antimony s-character and iodine p-character whereas the conduction band state is mainly antimony p-character. The Va_{Rb} defect iso-surface (Fig. 5(c)) is also delocalized, particularly along crystallographic (c,b) plane, where its charge distribution is very similar to that of the valence band edge state indicating strong coupling with the valence band states which are close in energy. The vacancy is located in the lower layer of the supercell while the defect state distributes over both layers indicating strong defect hybridization with the valence band state. The Rb_i has a delocalized defect iso-surface (not shown) similar to the conduction band edge state. These delocalized defect states are consistent with the shallow defect levels for V_{Rb} and Rb_i reported in Fig. 3 and S4. In contrast, the V_{I1} defect iso-surface (Fig. 5(d)) is very well localized within one of the layers of $[SbI_6]^{-3}$ octahedra, with charge mainly on the antimony dangling bond site, but some stretches over to neighboring *Sb* and *I* atoms.

As discussed in the next section, for experimental conditions, the

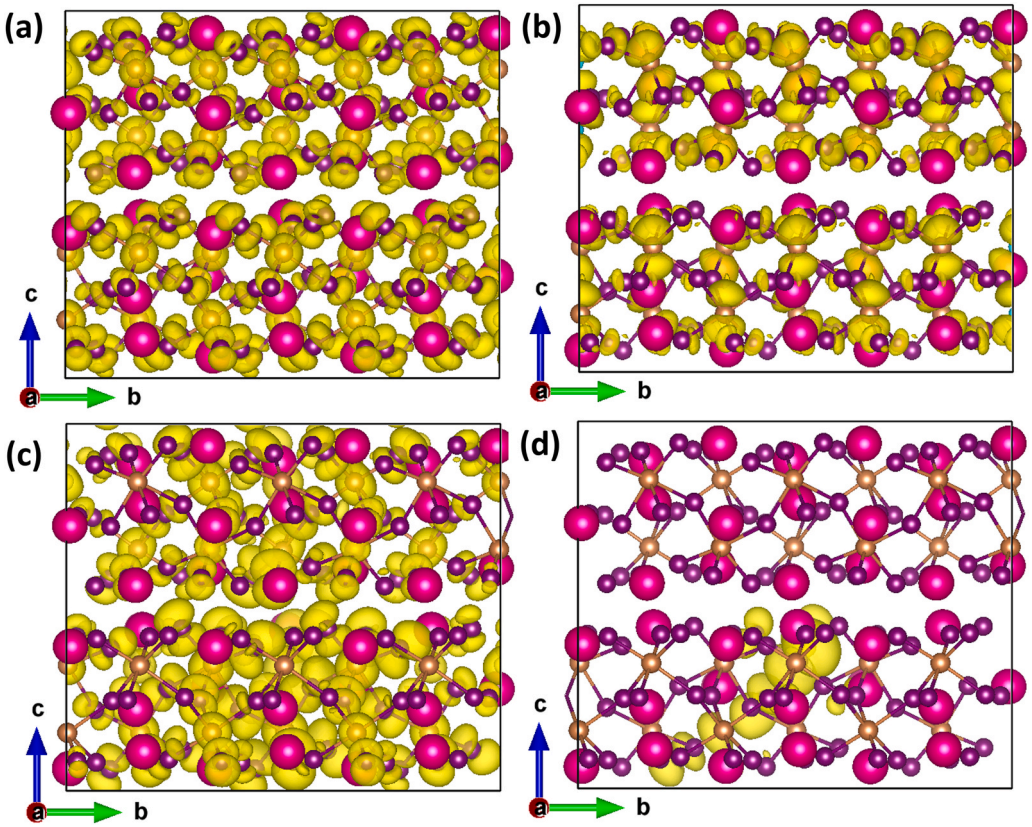

Fig. 5. Superimposed on the ball-and-stick supercell model is the defect level charge iso-surfaces for (a) the valence band maximum state, (b) the conduction band minimum state, (c) the defect state for rubidium vacancy (Va_{Rb}) and (d) the occupied defect level for the iodine vacancy (Va_{I1}). The yellow charge iso-surfaces are for an electron charge density of $1.5x10^9\ cm^{-3}$. (For interpretation of the references to colour in this figure legend, the reader is referred to the Web version of this article.)

iodine vacancy (Va_{I1}), the rubidium vacancy (Va_{Rb}) and the rubidium interstitial (Rb_{i1}) are the lowest energy defects, and therefore the most common defects. These three defects have been examined in more detail. Specifically, using a $1 \times 2 \times 1$ supercell, the properties of these defects are calculated at both the PBEsol and HSE-SOC levels of theory. The shallow defects (Va_{Rb} & Rb_{i1}) are similar for both PBEsol and HSE-SOC calculations whereas the iodine vacancy shows a larger energy splitting of the occupied and empty defect levels. Semi-local exchange methods (such as PBEsol) tend to de-localize the charge of deep defects which can result in unrealistic relaxations and inaccurate formation energies [38]. In Fig. 6, we compare the PBEsol and HSE-SOC defect levels and spin density results for the (Va_{I1}) iodine vacancy using the $1 \times 2 \times 1$ supercell. Fig. 6(a) shows the occupied-unoccupied defect level splitting is larger by $\approx 0.6\ eV$ in the HSE-SOC compared to the semi-local (PBEsol) result. Despite differing levels in the gap, the defect states have very similar localized charge-structure illustrated in Fig. 6(b) indicating PBEsol mainly captures the electronic and physical features of the defect state.

4.2. formation energies

From $2 \times 3 \times 1$ supercell, PBEsol energy calculations, we determine the formation energies for each defect in various charge states. In Fig. 7, the defect formation energies for each defect are plotted as a function of the Fermi energy. See Section II (Methods) for a discussion of the defect formation energy. For each intrinsic defect considered, only the charge state with the lowest energy at a given Fermi value is plotted in Fig. 7. The slope of the lines plotted indicates the lowest energy charge state. The Fermi energy varies from 0 to the theoretical band gap energy of 2.07 eV. The vacancy defects are shown in red, the iodine interstitials are in green, the rubidium interstitials are in blue and the antimony interstitials are in yellow. The anti-site defects are not shown in Fig. 7 as they are higher at the important mid-gap Fermi levels and wont be experimentally relevant. In supplemental section Fig. S4, we reproduce Fig. 7 but adding anti-site defects.

Fig. 7 determines the lowest energy, physically relevant charge state for each defect for each value of the Fermi energy. Antimony (Sb) ions are found in the +3 ionic state in bulk $Rb_3Sb_2I_9$. Therefore, it is sensible that Sb interstitials in the +3 charge state are the lowest energy defects in heavily p-type samples (i.e. when the Fermi energy is near the valence band edge and defects can easily exchange electrons with the low Fermi level) whereas Sb vacancies in the −3 charge state are the lowest energy defects in heavily n-type samples. Typically, extrinsic substitutional defects are not used to dope $Rb_3Sb_2I_9$ samples. Instead, the Fermi energy (E_F) is determined by the concentration of precursor molecules and conditions during growth. Also, charge neutrality for the sample requires the sum of all excess charges must cancel. Assuming thermodynamic equilibrium with the band edge states prevails, the Fermi energy E_F can be determined from the intrinsic defect formation energy results reported in Fig. 7 and the following charge neutrality equation:

$$0 = p - n + \sum n_j q_j \exp\left(-\frac{E^j_{form}}{k_B T}\right)$$

where n (p) is the additional band concentration of electrons (holes) and for the j^{th} defect, n_j is the site concentration taking into account degeneracy, q_j is the charge, E^j_{form} is the formation energy and the summation is over all defects considered. The n (p) values can be calculated from Boltzmann statistics given the Fermi energy is much greater than $k_B T$. Importantly, T is the temperature during the growth of the $Rb_3Sb_2I_9$ crystal which, based on recently reported processing temperatures [7], we take to be 225 °C. Since n, p and E^j_{Form} all depend on Fermi energy, the charge neutrality equation can be used to find the Fermi energy value where the concentration of negative charges cancels the positive charges in the crystal.

To find the Fermi level caused by intrinsic defects, one must choose the growth conditions which experimentally are based on molecular precursor concentrations but theoretically are determined by the values of chemical potentials ($\mu_{Rb}, \mu_{Sb}, \mu_I$) discussed in Section III(b). Specifically, we chose chemical values potential ($\Delta\mu_{Rb}, \Delta\mu_{Sb}, \Delta\mu_I$) of (−2.458, 0.0, −0.503) in eV. In the supplemental section Fig. S5, we show defect formation energy plots, such as Fig. 7, for other chemical potential values. From the results of Fig. 7, we determine our $E_F = E_{VBM} + 0.91\ eV$. This Fermi level result indicates that such a $Rb_3Sb_2I_9$ sample would be considered intrinsic, as found in recently grown samples [7].

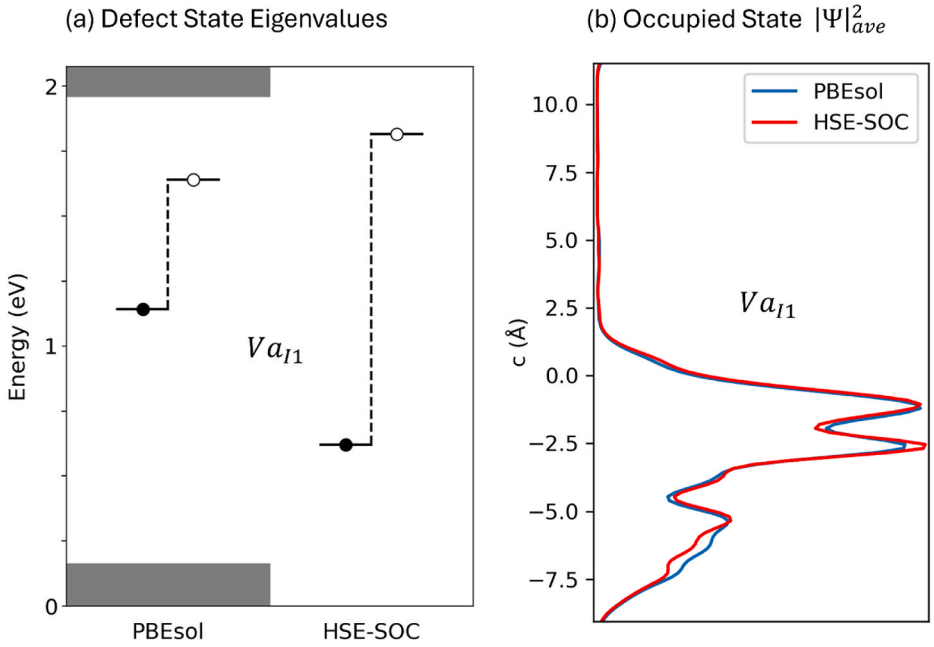

Fig. 6. Plots of the eigen-levels for the Va_{I1} neutral defect in between the valence band maximum and conduction band minimum from PBEsol and HSE-SOC calculations. Filled circles are occupied states and open circles are unoccupied states. The grey region shows the band edge differences between the PBEsol and HSE-SOC calculations.

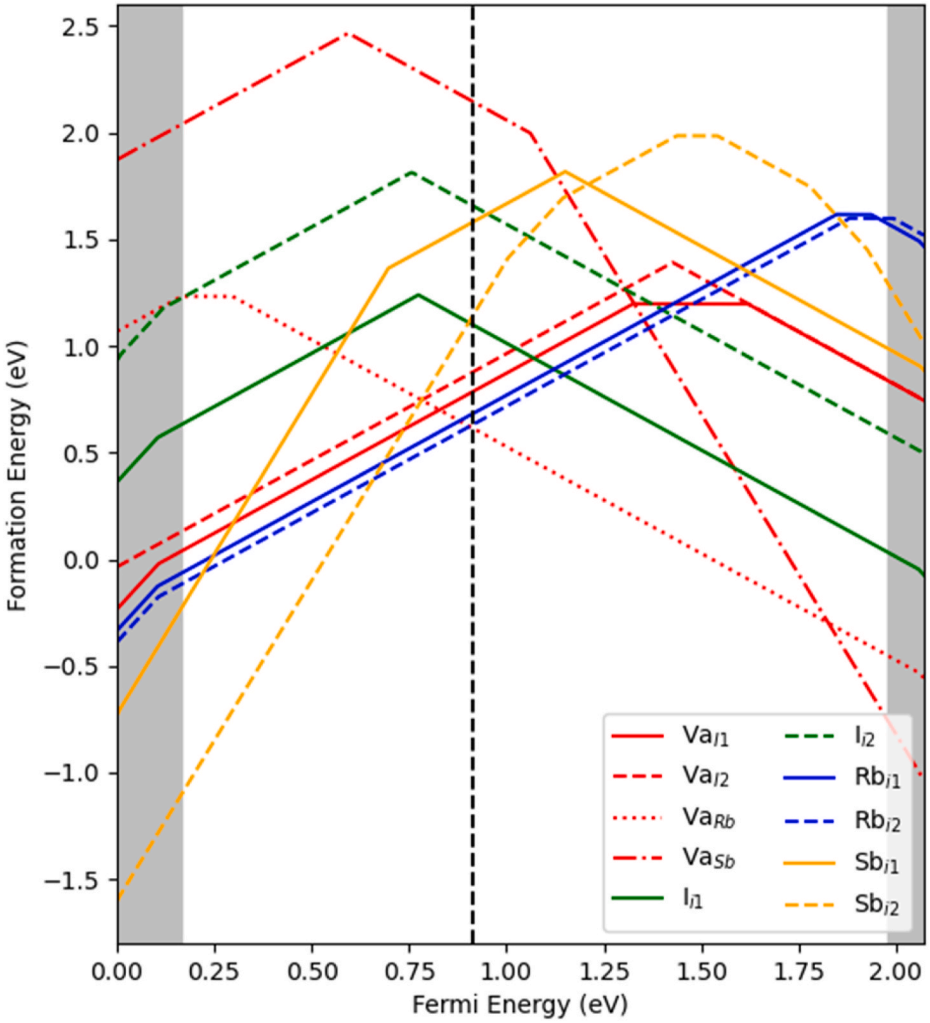

Fig. 7. Defect formation energies are plotted versus the Fermi energy, which varies across the band gap. Calculations employ a 2 × 3 × 1 supercell and PBEsol. In the grey area, the PBEsol energy results are extended based on the HSE06-SOC band edge offsets. The chemical potential values ($\Delta\mu_{Rb}, \Delta\mu_{Sb}, \Delta\mu_I$) values used correspond to point D on Supplemental Fig. S3b. The vertical dashed black line represents the Fermi level as determined by charge neutrality considerations.

The equilibrium Fermi energy is slightly to the right of crossing between the lowest energy +1 charge defect (Rb_i) and the lowest energy − 1 charge defect (Va_{Rb}).

From Fig. 7, the lowest formation energy defects at the "intrinsic" E_F value will have the largest concentrations. Therefore, rubidium vacancy (Va_{Rb}) in the minus 1 charge state will be most common with a concentration close to 10^{17} cm^{-3}. We estimate there will be one rubidium vacancy for every million rubidium atoms. Then, the next most common defects are the +1 charged rubidium interstitials (Rb_i) and iodine vacancies (Va_I). Specifically, the Rb_i^{+1} concentration is predicted to be about 93% of the Va_{Rb}^{-1} concentration. There will be an electrostatic and potential energetic attraction between these two defects and there may be circumstances where these defects recombine. The concentration of Va_I^{+1} is about 7 % of the Va_{Rb}^{-1} concentration. Other defects (I_i^{+1} and Sb_i^{+3}) have concentrations less than 1 % of the Va_{Rb}^{-1} concentration.

The results reported in Fig. 7 are all calculated using a 2 × 3 × 1 supercell and the PBEsol method. For the lowest energy defects identified (Va_{Rb}, Va_I, Rb_i) we have calculated the formation energies within a 1 × 2 × 1 supercell using both the PBEsol and HSE-SOC method and the formation energy results are reported in Fig. 8(a) and (b), respectively. For both cases, the chemical potential is chosen to correspond (using the appropriate method) to the value used for Fig. 7 so the results are directly comparable. The intrinsic Fermi level results are very similar; in Fig. 8(a) the PBEsol 1 × 2 × 1 supercell calculations result in E_F = 0.81 eV whereas in Fig. 8(b) for HSE-SOC we find E_F = 0.80 eV. For the iodine vacancies, the PBEsol results in Fig. 7 for the 2 × 3 × 1 supercell show slightly less deviation between the Va_{I1}^{+1} and Va_{I2}^{+1} energies when compared to the respective PBEsol results in Fig. 8(a) for the 1 × 2 × 1 supercell. In contrast, the HSE-SOC results for the 1 × 2 × 1 supercell in Fig. 8(b) find the Va_I^{+1} energy is ≈ 0.8 eV lower for site 1. Since both Va_{Rb} and Rb_i are shallow defects and other deep defects are significantly higher in energy, Va_{I1} is the strongest candidate for defect assisted recombination in $Rb_3Sb_3I_9$-based devices.

4.3. recombination energetics

Configuration coordinate diagrams (CCDs) allow us to estimate the charge transition energetics due to radiative or non-radiative processes [25,26]. Specifically, we will employ CCDs to explain cathode-luminescence [10], photo-luminescence [13] and photo-conductivity transient spectra [11]. See Ref. [25] for a detailed description of CCDs. In brief, CCDs show the relative energy between two defect charge states as a function of a general configuration coordinate (Q), which is a one-dimensional measure of the displacements of all atoms as the system moves from one charge configuration state to another. In Fig. 9, we report the CCD of the iodine vacancy (V_{I1}) using the q = 0 charge state as the reference where Q = 0 and E = 0. In Fig. 9, the iodine vacancy is switching between the q = −1 to the neutral q = 0

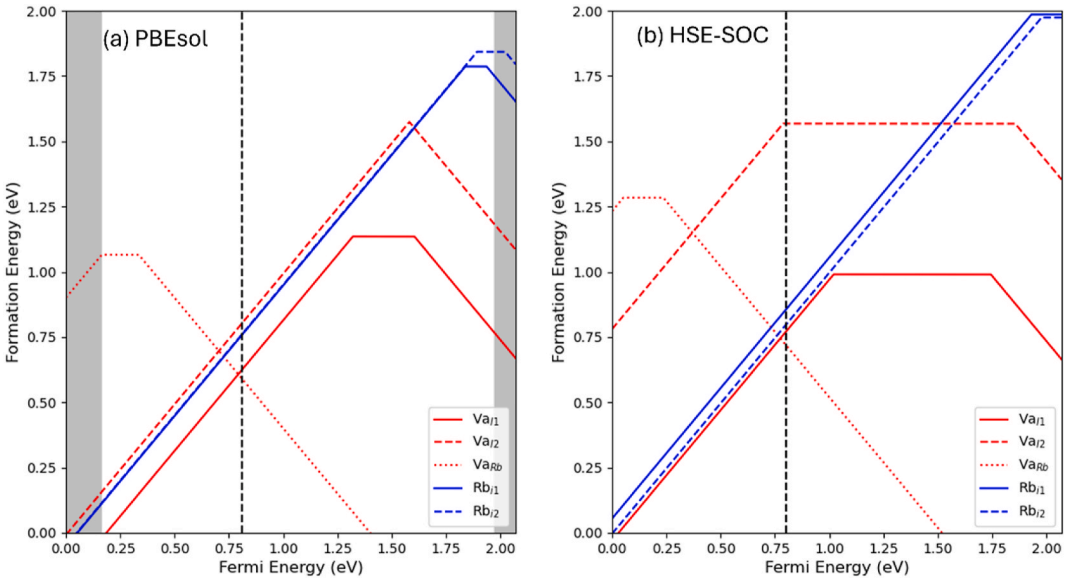

Fig. 8. Defect formation energies are plotted versus the Fermi energy for (a) PBEsol, which varies across the band gap. Calculations employ a $1 \times 2 \times 1$ supercell and (a) PBEsol and (b) HSE-SOC. In (a), the PBEsol energy results are extended based on the HSE06-SOC band edge offsets. The chemical potential values ($\Delta\mu_{Rb}, \Delta\mu_{Sb}, \Delta\mu_I$) values used correspond to point D on respective figure in supplemental section S3. The vertical dashed black line represents the Fermi level as determined by charge neutrality considerations.

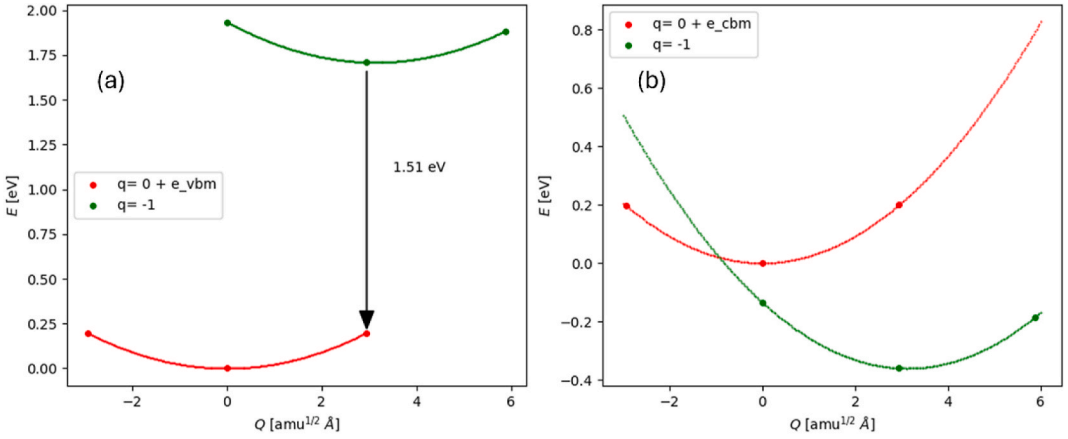

Fig. 9. Configuration coordinate diagram for iodine vacancy of type 1 with the defect reference state having neutral charge for (a) an extra electron in the valence band maximum energy state (e_vbm). The dots are calculated data points which are smoothly fit with a 2^{nd} order polynomial shown as the solid curves. Energies are calculated for $1 \times 2 \times 1$ supercells using the HSE-SOC method (PBEsol versions are shown in the supplemental section Fig. S5).

charge state. At $Q \approx 3$ $\left[amu^{1/2}\,\text{Å}\right]$ the $q = -1$ vacancy is in its lowest energy state. In Fig. 9(a), the $q = -1$ minimum energy value is 1.71 eV above the reference energy of the vacancy in the $q = 0$ state, plus an electron in a valence band maximum energy state.

Fig. 9 allows us to understand the recombination processes that occur at an iodine vacancy during a luminescence or photo-conductivity experiment in which electron-hole pairs are formed in large numbers. Almost all V_I defects are initially positively charged as indicated by Figs. 7 and 8. This initial $q = +1$ state will attract photo-induced electrons and repel holes. A large fraction will become negatively charged. Fig. 9(b) shows that an electron in the conduction band can be captured by the neutral iodine vacancy by a nearly barrierless process. Then, a free hole in valence band is attracted to and can recombine with the negatively charged Va_{I1} defect; the radiative process is illustrated in Fig. 9(a) by the vertical arrow. A full calculation of the luminescence spectra is possible [25] but beyond the scope of the present study. From Fig. 9(a), we predict a luminescence experiment would find an emission spectra centered at $E^{th}_{Lum} = 1.51\ eV$. This value is also found in our PBEsol calculations as shown in Supplemental Fig. S5. Zero point and thermal motion in addition to quantum tunneling effects may alter the luminescence peak values from the calculated value here. One cathode-luminescence experiment finds the defect related luminescence spectra can be deconvolved into distinct peaks with the main defect related feature peaking at 1.63 eV [10]. Similarly, another photo-luminescence study reports a single broad defect feature centered at 1.6 eV [13].

In $Rb_3Sb_2I_9$ photo-induced conductivity transient (PICT) experiments [11], a voltage is placed across the sample so free electrons and holes are quickly removed and the final transient conductivity is due to de-trapping of near band edge defect which we propose are Va_{I1}^{-1} defects. The CCD for this situation is represented in Fig. 9(b), where a negatively charged V_{I1} defect no longer has a free hole to recombine with. In this case, the electron trapped in the V_{I1}^{-1} defect must increase its state energy through multi-phonon excitation in order to release an electron into the conduction band. The minimum barrier energy to be overcome is 0.36 eV. Experimentally, data is fitted to an Arrhenius curve at elevated

temperatures in which case the extracted barrier is generally larger than the minimum by as much as $\approx 0.2\ eV$, depending on the CCD involved [39]. From our CCD results, we predict the Va_{I1}^{-1} trap level measured in an $Rb_3Sb_2I_9$ PICT experiment to be $E_{PICT}^{th} > 0.4\ eV$. Experiments find a single PICT trap level in $Rb_3Sb_2I_9$-devices where in one sample, $E_{PICT}^{exp} = 0.62\ eV$, and in another, $E_{PICT}^{exp} = 0.53\ eV$ [11].

5. Discussion and conclusion

In this study, we use *ab initio* density functional calculations to determine the properties of bulk $Rb_3Sb_2I_9$ with a focus on intrinsic point defects. We determine the structural and electronic properties of all intrinsic defects including vacancies, interstitials and anti-site substitutional defects. In Figs. 7 and 8, we report the Fermi level dependent formation energies relevant to recently grown samples. The most common defects in as-grown samples are expected to be Va_{I1}^{+1}, Va_{Rb}^{-1} and Rb_i^{+1}.

An important aspect of this work is the semi-quantitative agreement between the present atomic level theory and several experiments. We predict Va_{Rb} and Rb_i have shallow gap states that couple efficiently to nearby band edge states (see Figs. 4 and 5). In microcrystalline samples, these states may not significantly trap carriers. In addition, the Va_{Rb} and Rb_i defects may be difficult to distinguish from band tail states or the self-trapped holes that emerge during a luminescence experiments. In Fig. 9, we report our HSE-SOC iodine vacancy energy configuration coordinate diagram calculations. The energy predictions from these calculations agree with previously reported experimental results, including photo-induced current transient spectra [11] as well as cathodoluminescence [10] and photo-luminescence [13].

New measurements would help test the Va_{I1} model proposed here. Fig. 9 shows results for transition between the $q = -1$ and neutral charge state of the Va_{I1} defect. We predict (see Supplemental Fig. S6) the neutral to $q = +1$ radiative transition would have $E_{Lum}^{th} \approx 0.5\ eV$, which may be observable. For this transition, the classical barrier for non-radiation recombination is only $\approx 0.3\ eV$ so non-radiative transitions may reduce the luminescence intensity. Also, electrically detected magnetic resonance [40] would help characterize the atomic nature of defect-enhanced recombination and would be a nice test of the iodine vacancy theory presented here.

Iodine vacancies are predicted to be the main source of defect-enhanced recombination. New processing methods should be developed to limit these defects. In the above analysis, the concentration of defects is assumed to be mainly controlled by equilibrium thermodynamics under a specific growth condition where the Fermi energy is controlled by the charge neutrality condition and intrinsic defects. One processing strategy for reducing the deleterious iodine vacancies would be to extrinsically raise the Fermi energy by n-type doping with heterovalent impurities. We estimate that raising the Fermi energy by 0.1 eV would reduce the iodine vacancy concentration by an order of magnitude. This would also increase the rubidium vacancy concentration, but these defects may be benign. Another strategy is introducing excess iodine during a post-deposition annealing step. This strategy would need to be implemented with care to avoid iodine interstitials from combining with the common rubidium vacancies to form I_{Rb} defects. Our calculations show that I_{Rb} defects are fast recombination centers (see Fig. S7 in the supplemental section) which would be more deleterious than iodine vacancies. Despite the challenges involved, reducing iodine vacancies should be pursued to extend the carrier lifetime of $Rb_3Sb_2I_9$ semiconductors.

In summary, this work provides atomic-level information of intrinsic defects which provide mechanistic insights into diverse experimental observations of defects in $Rb_3Sb_2I_9$ bulk crystals. By determining the origin and energy levels associated with defects that act as recombination centers, we identify the optoelectronic bottlenecks that may limit the carrier lifetimes. Leveraging these insights, we provide guidance on potential strategies to mitigate the impact of these defects and to help realize the full potential of $Rb_3Sb_2I_9$ in optoelectronic and other device applications.

CRediT authorship contribution statement

Blair R. Tuttle: Writing – review & editing, Writing – original draft, Visualization, Validation, Supervision, Resources, Project administration, Methodology, Investigation, Funding acquisition, Formal analysis, Data curation, Conceptualization. **Evan J. Payne:** Writing – review & editing, Visualization, Software, Investigation, Formal analysis, Data curation. **Zachery J. Willard:** Writing – review & editing, Visualization, Software. **Sanjay V. Khare:** Writing – review & editing, Resources, Funding acquisition. **Vincenzo Pecunia:** Writing – review & editing, Conceptualization.

Declaration of competing interest

The authors declare the following financial interests/personal relationships which may be considered as potential competing interests: Blair Tuttle reports financial support was provided by National Science Foundation. If there are other authors, they declare that they have no known competing financial interests or personal relationships that could have appeared to influence the work reported in this paper.

Acknowledgements

BRT gratefully acknowledges support from National Science Foundation under grant DMR-2127473. Computations for this research were performed on the Pennsylvania State University's Institute for Computational and Data Sciences' Roar Collab supercomputer. ZW, EP and SVK gratefully acknowledge support from the University of Toledo's Physics Research Experiences for Undergraduates (REU) program funded by NSF Grant #2349585.

Appendix A. Supplementary data

Supplementary data to this article can be found online at https://doi.org/10.1016/j.jpcs.2025.113190.

Data availability

Data will be made available on request.

References

[1] V. Pecunia, et al., Roadmap on energy harvesting materials, J. Phys.: Materials 6 (4) (2023/08/07 2023) 42501.
[2] A.K. Jena, A. Kulkarni, T. Miyasaka, Halide perovskite photovoltaics: background, status, and future prospects, Chem. Rev. 119 (5) (2019/03/13 2019) 3036–3103.
[3] G. K. Grandhi et al., "Wide-bandgap perovskite-inspired materials: defect-driven challenges for high-performance optoelectronics," Adv. Funct. Mater., vol. n/a, no. n/a, p. 2307441.
[4] A. Chakraborty, N. Pai, J. Zhao, B.R. Tuttle, A.N. Simonov, V. Pecunia, Rudorffites and beyond: perovskite-inspired silver/copper Pnictohalides for next-generation environmentally friendly photovoltaics and optoelectronics, Adv. Funct. Mater. 32 (36) (2022) 2203300.
[5] K. Ahmad, S.M. Mobin, Recent progress and challenges in A3Sb2X9-based perovskite solar cells, ACS Omega 5 (44) (2020/11/10 2020) 28404–28412.
[6] Z.X. Jin, Z. Zhang, J.W. Xiu, H.S. Song, T. Gatti, Z.B. He, A critical review on bismuth and antimony halide based perovskites and their derivatives for photovoltaic applications: recent advances and challenges, J. Mater. Chem. A 8 (32) (Aug 2020) 16166–16188.
[7] F. Li, Y. Wang, K. Xia, R.L.Z. Hoye, V. Pecunia, Microstructural and photoconversion efficiency enhancement of compact films of lead-free perovskite derivative Rb3Sb2I9, J. Mater. Chem. A 8 (8) (2020) 4396–4406, https://doi.org/10.1039/C9TA13352F.
[8] R.H. Ashwath, C. Sudakar, Diamond-shaped Rb3Sb2I9 microcrystals: structural and optical properties, Cryst. Growth Des. 25 (5) (2025/03/05 2025) 1466–1476.
[9] N. Lamminen, et al., Triple A-site cation mixing in 2D perovskite-inspired antimony halide absorbers for efficient indoor photovoltaics, Adv. Energy Mater. 13 (4) (Jan 2023).

[10] P.C. Harikesh, et al., Rb as an alternative cation for templating inorganic lead-free perovskites for solution processed photovoltaics, Chem. Mater. 28 (20) (Oct 2016) 7496–7504.
[11] V. Pecunia, et al., Assessing the impact of defects on lead-free perovskite-inspired photovoltaics via photoinduced current transient spectroscopy, Adv. Energy Mater. 11 (22) (2021) 2003968.
[12] J.-P. Correa-Baena, et al., A-site cation in inorganic A3Sb2I9 perovskite influences structural dimensionality, exciton binding energy, and solar cell performance, Chem. Mater. 30 (11) (2018/06/12 2018) 3734–3742.
[13] J. Mei, M. Liu, P. Vivo, V. Pecunia, Two-dimensional antimony-based perovskite-inspired materials for high-performance self-powered photodetectors, Adv. Funct. Mater. 31 (50) (2021) 2106295.
[14] K.M. McCall, et al., α-Particle detection and charge transport characteristics in the $A_3M_2I_9$ defect perovskites (A = Cs, Rb; M = Bi, Sb), Acs Photonics 5 (9) (Sep 2018) 3748–3762.
[15] C. Polyzoidis, K. Rogdakis, E. Kymakis, Indoor perovskite photovoltaics for the internet of things—challenges and opportunities toward market uptake, Adv. Energy Mater. 11 (38) (2021) 2101854.
[16] I. Mathews, S.N. Kantareddy, T. Buonassisi, I.M. Peters, Technology and market perspective for indoor photovoltaic cells, Joule 3 (6) (2019) 1415–1426.
[17] X. Chen, et al., Indoor photovoltaic materials and devices for self-powered internet of things applications, Mater. Today Energy 44 (2024/08/01/2024) 101621.
[18] K.M. McCall, C.C. Stoumpos, S.S. Kostina, M.G. Kanatzidis, B.W. Wessels, Strong electron-phonon coupling and self-trapped excitons in the defect halide perovskites $A_3M_2I_9$ (A = Cs, Rb; M = Bi, Sb), Chem. Mater. 29 (9) (May 2017) 4129–4145.
[19] J.-H. Chang, T. Doert, M. Ruck, Structural variety of defect perovskite variants M3E2X9 (M = Rb, Tl, E = Bi, Sb, X = Br, I), Z. Anorg. Allg. Chem. 642 (13) (2016) 736–748.
[20] V. Pecunia, Efficiency and spectral performance of narrowband organic and perovskite photodetectors: a cross-sectional review, J. Phys.: Materials 2 (2019) 42001.
[21] P. Hohenberg, W. Kohn, Inhomogeneous electron gas, Phys. Rev. 136 (3B) (1964) B864–B871.
[22] W. Kohn, L.J. Sham, Self-consistent equations including exchange and correlation effects, Phys. Rev. 140 (4A) (1965) A1133–A1138.
[23] J.P. Perdew, K. Burke, M. Ernzerhof, Generalized gradient approximation made simple, Phys. Rev. Lett. 77 (18) (1996) 3865–3868.
[24] J.P. Perdew, et al., Restoring the density-gradient expansion for exchange in solids and surfaces, Phys. Rev. Lett. 100 (13) (2008) 136406.
[25] A. Alkauskas, M.D. McCluskey, C.G. V.d. Walle, Tutorial: defects in semiconductors—combining experiment and theory, J. Appl. Phys. 119 (18) (2016) 181101.
[26] C. Freysoldt, et al., First-principles calculations for point defects in solids, Rev. Mod. Phys. 86 (1) (2014) 253–305.
[27] C.G. Van de Walle, J. Neugebauer, First-principles calculations for defects and impurities: applications to III-nitrides, J. Appl. Phys. 95 (8) (2004) 3851–3879.
[28] C. Freysoldt, J. Neugebauer, C.G. Van de Walle, Fully ab initio finite-size corrections for charged-defect supercell calculations, Phys. Rev. Lett. 102 (1) (2009) 16402.
[29] Y. Kumagai, N. Tsunoda, A. Takahashi, F. Oba, Insights into oxygen vacancies from high-throughput first-principles calculations, Phys. Rev. Mater. 5 (12) (2021) 123803.
[30] C. Freysoldt, J. Neugebauer, C.G. Van de Walle, Electrostatic interactions between charged defects in supercells, physica status solidi (b) 248 (5) (2011) 1067–1076.
[31] K. Momma, F. Izumi, VESTA 3 for three-dimensional visualization of crystal, volumetric and morphology data, J. Appl. Crystallogr. 44 (6) (2011) 1272–1276.
[32] J. Heyd, G.E. Scuseria, M. Ernzerhof, Hybrid functionals based on a screened Coulomb potential, J. Chem. Phys. 118 (18) (2003) 8207–8215.
[33] J. Heyd, G.E. Scuseria, M. Ernzerhof, "Erratum: “Hybrid functionals based on a screened Coulomb potential”, J. Chem. Phys. 118 (2003) 8207. " The Journal of Chemical Physics, vol. 124, no. 21, p. 219906, 2006.
[34] S. Steiner, S. Khmelevskyi, M. Marsmann, G. Kresse, Calculation of the magnetic anisotropy with projected-augmented-wave methodology and the case study of disordered ${\mathrm{Fe}}_{1\ensuremath{-}x}{\mathrm{Co}}_{x}$ alloys, Phys. Rev. B 93 (22) (2016) 224425.
[35] V.T. Barone, B.R. Tuttle, S.V. Khare, Properties of AgBiI4 using high through-put DFT and machine learning methods, J. Appl. Phys. 131 (24) (2022).
[36] Z. Xiao, W. Meng, D.B. Mitzi, Y. Yan, Crystal structure of AgBi2I7 thin films, J. Phys. Chem. Lett. 7 (19) (2016/10/06 2016) 3903–3907.
[37] M. Gajdoš, K. Hummer, G. Kresse, J. Furthmüller, F. Bechstedt, Linear optical properties in the projector-augmented wave methodology, Phys. Rev. B 73 (4) (2006) 45112.
[38] D. Wickramaratne, J.L. Lyons, Assessing the SCAN functional for deep defects and small polarons in wide band gap semiconductors and insulators, Phys. Rev. B 109 (24) (2024) 245201.
[39] D. Wickramaratne, et al., Defect identification based on first-principles calculations for deep level transient spectroscopy, Appl. Phys. Lett. 113 (19) (2018).
[40] K.J. Myers, P.M. Lenahan, J.P. Ashton, J.T. Ryan, A new approach to electrically detected magnetic resonance: spin-dependent transient spectroscopy, J. Appl. Phys. 132 (11) (2022).